Technical Physics, 2023, Vol. 68, No. 9

06

Influence of varistor effect and contact phenomena on the characteristics of solid-state lithium-ion batteries with semiconductor electrodes

© *A.S. Rudy, A.A. Mironenko, V.V. Naumov, A.B. Churilov, S.V. Kurbatov, Yu.S. Egorova, E.A. Kozlov*

Valiev Institute of Physics and Technology of RAS, Yaroslavl Branch,
150007 Yaroslavl, Russia
e-mail: rudy@uniyar.ac.ru

Received May 5, 2023
Revised July 10, 2023
Accepted July 12, 2023

The results of measuring the charge-discharge characteristics of solid-state thin-film lithium-ion batteries with a nanocomposite anode based on a-Si(Al) solid solution are presented. The charging characteristics of batteries have a feature in the form of a step on the smooth branch of the charge curve. It is shown that the appearance of the step is associated with the compensation of a-Si(Al) and the change from hole to electron conductivity due to lithiation of the electrode during charging. As a result of lithiation, the electron over-barrier current becomes the main component of the charging current. To maintain a galvanostatic charge mode, the potentiostat increases the voltage by the height of the potential barrier, which leads to the appearance of a step on the charging curve. The impedance of a solid-state thin-film lithium-ion battery of the $LiCoO_2-LiPON-Si@O@Al$ electrochemical system was measured in the temperature range from -20 to 50°C. A structural model of the accumulator is proposed and the parameters of the structural elements of the model are calculated which provide the best fit for experimental Nyquist diagrams. The obtained values of the electrodes' resistivity are orders of magnitude higher than the results of direct measurements and data from literary sources. According to the IV-characteristics obtained by cyclic voltammetry the high resistance of the electrodes is due to the metal-semiconductor contact and the varistor effect of the electrode material. The results obtained make significant adjustments to the interpretation of the impedance spectra and structural models of solid-state lithium-ion batteries based on semiconductor materials.

Keywords: Thin-film solid-state lithium-ion battery, semiconductor, nanocomposite, impedance spectroscopy, Schottky barrier, varistor effect.

DOI: 10.61011/TP.2023.09.57363.120-23

Introduction

In the last two decades, in parallel with the production of lithium-ion batteries with liquid electrolyte, intensive development of solid-state thin-film lithium-ion batteries (SSLIB) has taken place. It is generally accepted that the demand for SSLIB is driven by the development of micro and nanoelectronics devices, microelectromechanical systems, RFID tags and smart cards. However, it is evident from IDTechEx report that the growth of the SSLIB industry is primarily driven by the expanding market for miniature and wearable electronic devices such as smartphones, wrist-worn gadgets, and transdermal patches. Smartphones ($\sim 25\%$ of all SSLIB), wrist-worn gadgets ($\sim 30\%$) and transdermal patches ($\sim 25\%$) are the most widely used SSLIB, while SSLIB for RFID tags and smart cards account for less than 10% of the total. The SSLIB market is expected to grow from US$ 22 mln to US$ 109 mln from 2020 to 2025 and is expected to reach US$ 500 mln in 2030 [1].

The creation of SSLIB was made possible by the advent of the solid electrolyte — lithium phosphorus oxynitride or LiPON [2], which is used in virtually all modern industrial thin-film batteries. The popularity of LiPON is due to the fact that the lithium transfer number is almost equal to one, and SSLIB with LIPON are more technologically advanced, safer, and have high Coulomb efficiency. At the same time, the capacity of SSLIB is expectedly lower than that of batteries with liquid electrolyte. The main reasons — are the low conductivity of the solid electrolyte and the replacement of the percolation cluster of batteries with liquid electrolyte by an electrode-electrolyte interface that has a higher resistance.

All these features of SSLIB became clear back in the 2000 s when J. Bates and coworkers revealed the high resistance of the $LiPON-LiCoO_2$ [2] transition. The battery cells were incubated at 250° C for 10 min [2] to reduce the transition resistance. This research paved the way for a series of studies focused on reducing the internal resistance of SSLIB. The development of their structural models of SSLIB impedance became an integral part of such studies. The study objects were batteries of the most commercially successful electrochemical systems in which the negative electrode is made of lithium metal or graphite and the positive electrode — of lithium cobaltite or lithium ferrophosphate. These materials have a number of disadvantages, for example, the theoretical specific capacitance of graphite is relatively small and is only $372\,\mathrm{mA\cdot h/g}$. As for lithium, with a large theoretical capacity of $3828\,\mathrm{mA\cdot h/g}$, its practical capacity is only $380-800\,\mathrm{mA\cdot h/g}$. The reason lies in the encapsulation of lithium, i.e. the formation of a passivating film around lithium crystallites when charged. In addition, batteries with metallic lithium are not safe to use.

Silicon could be an alternative to carbon and lithium as it has the highest theoretical capacitance $4200\,\mathrm{mA \cdot h/g}$. In the last decade, a number of reviews have been published on the use of silicon in lithium-ion batteries [3–8]. But, since in all described cases of tests of silicon electrodes the number of charge–discharge cycles did not exceed two or three tens, the interest to this material is gradually decreasing. The problem is the rigidity of the silicon crystal structure, which breaks down when lithium is introduced long before the theoretical capacity is reached. To improve the stability of the silicon electrode, the authors developed a nanocomposite material Si@O@Al [9,10], which can withstand up to a thousand cycles of charge-discharge as part of the SSLIB. Subsequently, it was found that the Si@O@Al contact has a non-linear CVC [11], and as a composite material consisting of a semiconductor filler and a dielectric dispersant, Si@O@Al also has a varistor effect [12].

It should be noted that all promising electrode materials such as Si and its composites, $LiCoO_2$ and $Li_xV_2O_5$, belong to semiconductors. Of these, lithium cobaltite and vanadium pentoxide — are wide-band semiconductors whose Fermi level is below the Fermi level of the titanium used as the substrate and down condutor. Therefore, the down conductor contacts with $LiCoO_2$ and $Li_xV_2O_5$ are ohmic in the sense that there is no potential barrier at the metal–semiconductor interface. For example, the Ti–$LiCoO_2$ interface has an enriched electron layer, and although the electrons are minority charge carriers, the conductivity of the contact is $0.25\,\mathrm{S/cm^2}$. The work function for titanium is larger than for silicon ($A_{\mathrm{Ti}} > A_{\mathrm{Si}}$), so a Schottky barrier is formed at the Ti–Si interface, and both electrons and holes can be the main charge carriers depending on the degree of lithiation. In addition, electrode semiconductor materials are deposited by magnetron sputtering, resulting in porous nanocrystalline films. Such materials have a varistor effect, i.e., their conductivity depends on the current. These features of semiconductor electrode materials can not only affect the charging characteristics of SSLIB, but also lead to artefacts in impedance spectroscopy of SSLIB functional layers. The main effects associated with varistor and contact phenomena in semiconductor electrodes SSLIB are discussed below.

1. Fabrication of samples and methods of experimental studies

Experimental SSLIB samples with structure Ti(200 nm)—Si@O@Al(0.3 μm)—LiPON(1 μm)—$LiCoO_2$(1 μm)—Ti(10 μm) with area $1.44\,\mathrm{cm^2}$ and Ti(200 nm)—Si@O@Al(0.3 μm) —LiPON(1 μm)—$Li_xV_2O_5$%(1 μm)—Ti(10 μm) with area $7.9\,\mathrm{cm^2}$ were fabricated by magnetron sputtering using an SCR 651 Tetra (Alcatel) system. Mask technology was used for the deposition of functional layers, which allows to obtain test structures and films of individual functional layers simultaneously with SSLIB. The chemical composition of the targets, their sputtering and film deposition parameters are given in table 1. The ratio of gases in the mixtures is given in flow units. In the case of Si@O@Al films, the argon flux was maximized and the oxygen flux — minimized. To obtain amorphous structure, Si@O@Al nanocomposite was deposited at maximum magnetron power on cold substrate. Lithium-containing targets were sputtered at the highest possible power, i.e. the power above which cracking of the targets is possible. In parallel with the battery cells, Ti—Si@O@Al—Ti and Ti—$LiCoO_2$—Ti cells were fabricated to investigate the characteristics of the down conductor-electrode junction and so-called witnesses. The latter were used to determine the elemental and phase compositions of the functional layers of SSLIB.

Table 1. Process parameters of deposition of functional layers of SSLIB and test structures

Layer	Ti	$Li_xV_2O_5$	$LiCoO_2$	Si@O@Al	LiPON
Target	Ti	$Li_xV_2O_5$	$LiCoO_2$	Si_3Al	Li_3PO_4
Flow rate Ar, sccm	20	10	20	200	–
Flow rate O_2, sccm	–	1	5	0.6	–
Flow rate N_2, sccm	–	–	–	–	18
Ionic cleaning	–	15 V, 15 s	15 V, 15 s	15 V, 15 s	–
Residual pressure, Pa	0.2	0.23	1	1.75	0.2
Magnetron power, W	300	200	200	400	150
Deposition rate-nm/min	20	–	4.5	4	5.6
Thickness , nm	200	100	500	180	500

Scanning electron microscopy (SEM Supra 40, Quanta 3D 200i) and energy-dispersive microanalysis (INCAx-act and EDAX SEM attachments) were used to diagnose the functional layers of the SSLIB, test structures and witnesses. The phase composition of the functional layers was determined by X-ray diffraction analysis (XDA) on an ARL X'tra powder diffractometer. The battery cells proper were investigated by charge – discharge cycling and electrochemical impedance spectroscopy (EIS). The test structures were investigated by EIS and cyclic voltammetry to obtain the CVC of the junctions. Impedance measurements were performed using the four-point probe technique and an Elins P-40X single-channel potentiostat with an FRA-24M electrochemical impedance measurement module. The voltage amplitude was 5 mV, and the frequency range spanned from 500 kHz to 500 mHz. The impedance spectra

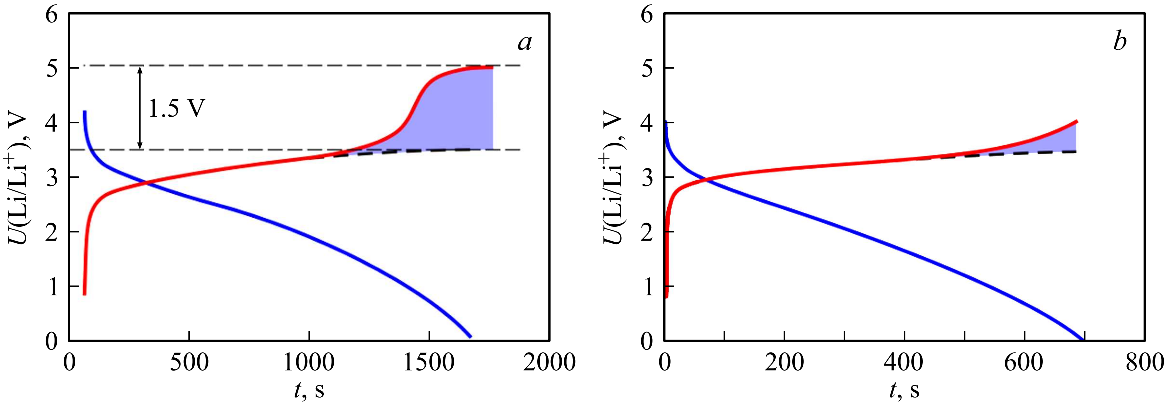

Figure 1. *a* — charge – discharge curve SSLIB Ti—Li$_x$V$_2$O$_5$—LiPON—Si@O@Al—Ti. Area $S = 7.9\,\mathrm{cm}^2$; 119th cycle; potential window 0−5 V; current $100\,\mu$ A. *b* — charged – discharge curve SSLIB Ti—LiCoO $_2$ —LiPON—Si@O@Al—Ti. Area $S = 1.44\,\mathrm{cm}^2$; 76th cycle; potential window 0−4 V; current $100\,\mu$A.

of Ti—Si@O@Al—Ti and Ti—LiCoO$_2$—Ti were recorded at offsets from 0 to 1 V in increments of 50 mV in a single pass from high frequency to low frequency.

2. Results and discussion

2.1. Effect of metal – semiconductor transition on charge curves of SSLIB

In the course of SSLIB cycling, it was found that at a high degree of lithiation, steps appear on the charge curves (Fig. 1, *a*), which are commonly referred to in the special literature as hikes [13]. Exactly the same steps were also observed in the SSLIB charge curves of the Ti—LiCoO$_2$—LiPON—Si@O@Al—Ti structure (Fig. 1, *b*). The simplest explanation for these features of the charge curves may be the formation of a Schottky barrier at the interface of the Si@O@Al nanocomposite and the titanium down conductor. Schottky barrier formation is directly related to the elemental composition of the Si@O@Al nanocomposite, which includes about 70% silicon, as well as 15 to 20% oxygen and 10 to 15% aluminium. The Si@O@Al films are X-ray amorphous and remain so during the charge – discharge [14] cycling process. The role of stabilizer of amorphous silicon phase (a-Si) in the nanocomposite is performed by aluminum, which, being in the nodes and interstices of the lattice, prevents crystallization of silicon during lithium extraction. In this case, the Si@Al system can be considered as a solid solution a-Si(Al), in which the solvent is amorphous silicon and the dissolved component — aluminum.

When silicon and aluminum are deposited on a cold substrate, an amorphous a-Si(Al) structure is formed, in which aluminum can occupy the positions shown in Fig. 2. For example, Al can occupy a position in the interstice of the crystal lattice and not form a chemical bond with Si (Fig. 2,*a*). In this case, a-Si(Al) is a solid solution In this case, a-Si(Al) is a solution an interstitial solid solution

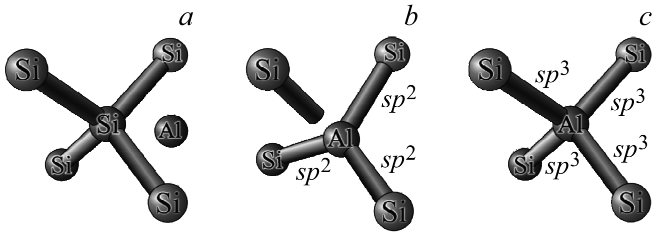

Figure 2. Possible ways of introducing aluminium into the silicon crystal lattice

In the strongly distorted sp^2 crystal lattice, hybridized Al can theoretically form the compound with silicon shown in Fig. 2, *b*, but there is no experimental evidence for such compounds. More likely is the excited sp^3-hybridized state of Al in which the bonds are directed to the vertices of the tetrahedron, which allows Al to be embedded in the silicon crystal lattice with minimal distortion of the latter (Fig. 2, *c*). The missing electron is captured from the orbital of the nearest silicon atom, resulting in the formation of a hole in the valence band of a-Si(Al). Thus, sp^3-hybridized aluminum is an acceptor impurity, and a-Si(Al) is a substitutional solid solution.

As an acceptor impurity for silicon [15], sp^3-hybridized Al significantly increases the hole concentration in the valence band. From data from direct measurements, the conductivity of Si@O@Al is $\sigma = en\mu = 3.19 \cdot 10^{-4}\,\mathrm{S \cdot m^{-1}}$, which implies that $n\mu = 1.99 \cdot 10^{15}\,\mathrm{S \cdot m^{-1} C^{-1}}$. That is, for a non-degenerate semiconductor with hole concentration $n \sim 10^{21}\,\mathrm{m}^{-3}$ mobility is $\mu \sim 10^{-6}\,\mathrm{m^2 (V \cdot s)^{-1}}$, which is two orders of magnitude higher than the mobility of charge carriers in a-Si. The high concentration of sp^3-hybridized Al and high hole mobility mean a low density of localized states. The minimum density value, as in hydrogenated silicon a-Si:H, can be $10^{21}–10^{22}\,\mathrm{eV^{-1} \cdot m^{-3}}$. Therefore, it is further assumed that the Fermi level of a-Si(Al) is not

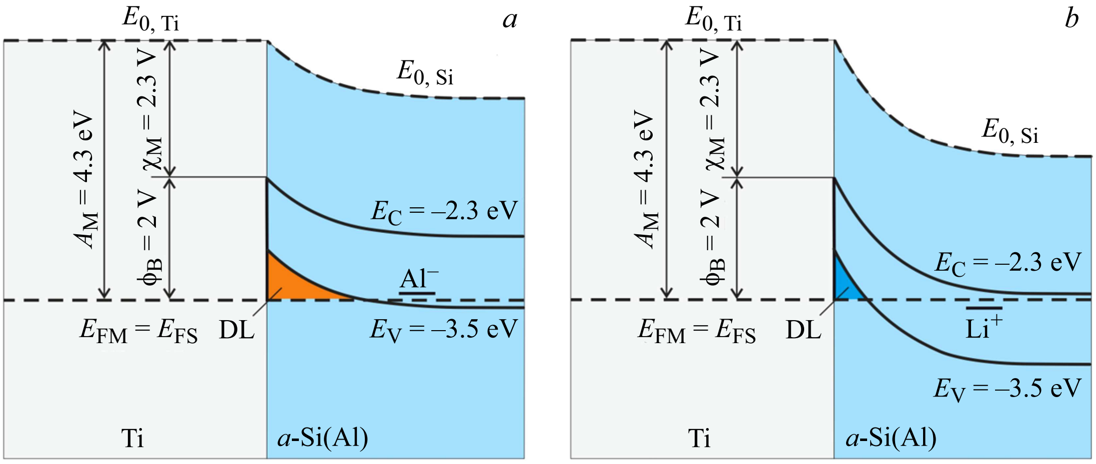

Figure 3. Zone structure of *a*-Si(Al)–Ti: contact: *a* — unlithiated (hole)*a*-Si(Al); *b* — lithiated (electron) *a*-Si(Li). A_M — titanium work function; χ — electron affinity; E_{FM} — Fermi level of titanium; E_{FS} — the Fermi level of amorphous silicon; E_C, E_V — mobility threshold energies (relative to vacuum); DL — the nucleated layer.

fixed and changes upon lithiation as the donor impurity of Al is compensated by lithium, i.e. in according to [15] — from the ceiling of the valence band to the bottom of the conduction band (Fig. 3).

In the energy band diagram shown in Figure 3, the boundaries of the conduction band and valence band are -2.3 and -3.5 eV respectively. These data are taken from [16], where the results of calculations of band-tail states using a large and realistic *a*-Si model of 4096 atoms (a cube with a side of about 43 Å) are given. Exactly the same results were obtained in [17] by the method described in [18], for a more plain model of 16 atoms. The use of the results of [16,17], which do not take into account the dissolved components, is quite acceptable, because the zone structure of amorphous silicon is determined by the short-range order of the crystal lattice, which does not change when introducing Al (Fig. 2, *a, c*). Dissolved components can only affect the density of localized states and the concentration of charge carriers. For example, sp^3-hybridized aluminum, unlike hydrogen in hydrogenated silicon, not only reduces the density of localized states but also increases the hole concentration. The titanium work function, shown in Fig. 3, is an average of experimental values lying in the range from 4.14 to 4.54 eV. This data discrepancy is due to the dependence of the work function on surface cleanliness. In Fig. 3, the Fermi level corresponds to an average work function value of 4.3 eV.

At the qualitative level, the explanation of the Schottky barrier effect on the charge curve is as follows. At low lithium concentration, *a*-Si(Al) is an *p*-type semiconductor, and its contact with Ti when charged is ohmic and directly biased (minus to Ti). Two kinds of charge carriers — electrons and holes flow through Si@O@Al. At the Ti-a-Si(Al) boundary, holes recombine with metal electrons, and the semiconductor electrons reduce lithium ions at the *a*-Si(Al)—LiPON boundary. The electron current is small due to the low electron concentration in *a*-Si(Al) and the presence of Schottky barrier at the interface, so the reduction of lithium ions at the interface *a* Si(Al)—LiPON occurs mainly due to the capture of valence electrons and the formation of holes in the valence band. The charge is then transferred by holes, which recombine at the Ti boundary, creating a recombination current. In this case, the voltage drop across the contact is small and there is no step in the charging curve.

Upon further charging, lithiation of the Si@O@Al nanocomposite and gradual compensation of the acceptor impurity Al, occurs followed by the change of the main charge carriers. The Ti—a-Si(Li) contact becomes a rectifying contact because the current through the contact is generated by electrons overcoming the Schottky barrier on the metal side. Since charging occurs in galvanostatic mode, to maintain a constant current, the charger increases the voltage by the Schottky barrier value to maintain a constant current, resulting in a step on the charge curve. Note that the height of the Schottky barrier on the metal side, determined by the Schottky–Mott rule $q\varphi_B = A_M - q\chi$, where χ — electron affinity, is independent of the Fermi level of the semiconductor. Therefore, the gradual manifestation of the barrier as a step is only due to the change in the conduction type of the nanocomposite. For titanium work function of 4.3 eV and electron affinity $\chi = 2.3$ V, the barrier height should be 2.0 V.

The step height in figure 1, *a* is 1.5 V, which is 0.5 V less than the Schottky barrier height shown in the energy band diagram *3*. The most likely reasons for the lowering of the barrier could be the Schottky effect due to electric image forces and the presence of surface states of amorphous silicon. Another reason could be the double electrical layer. When charged, lithium ions can form a double electric layer in the contact area, creating a field that coincide in

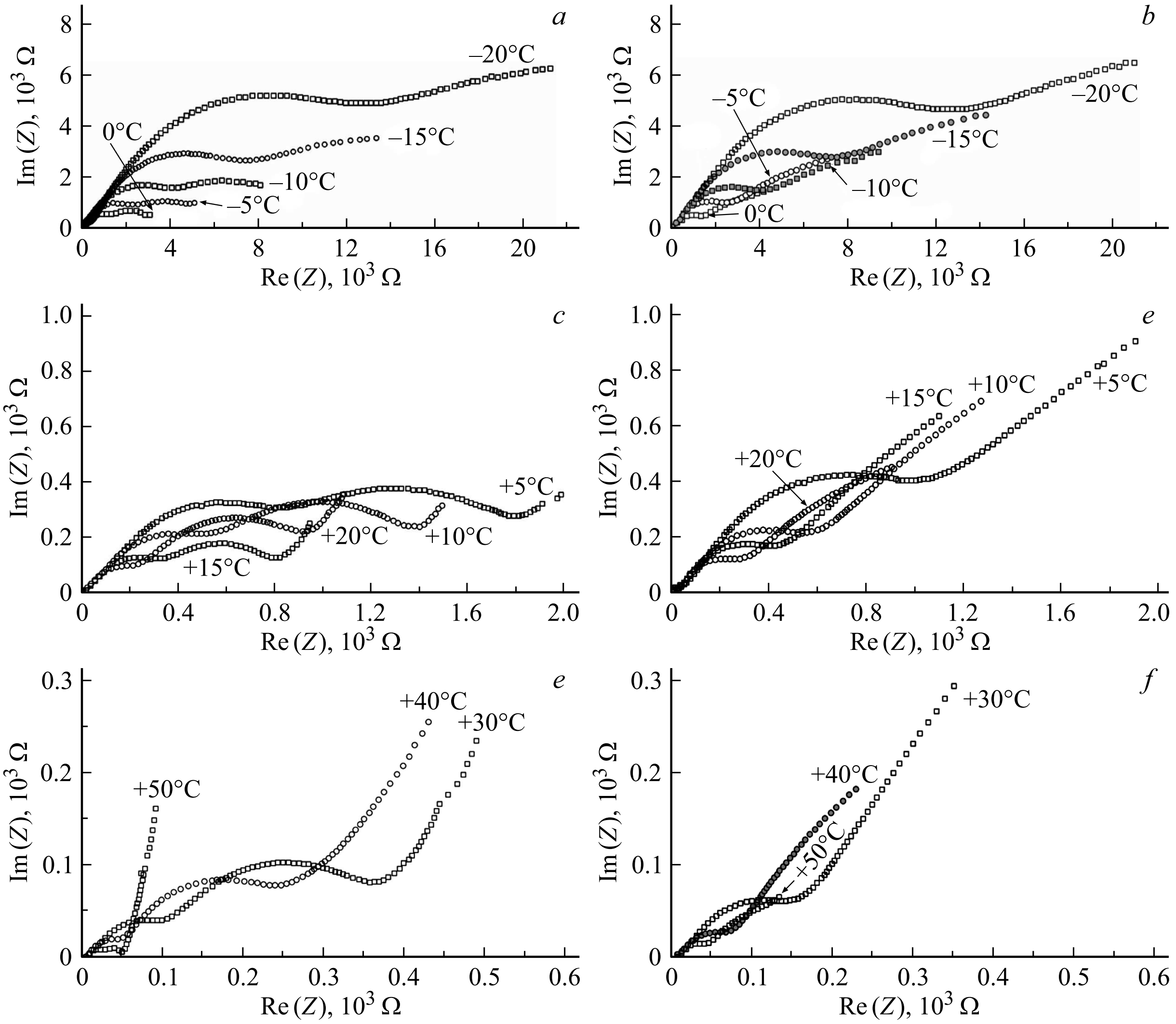

Figure 4. Impedance spectra of SSLIB Ti—LiCoO$_2$—LiPON—Si@O@Al—Ti in the temperature range from −20 to +50°C. *a, c, e* — in the charged state; *b, d, f* — in the discharged state.

direction with the image force field. Due to all of the above factors, there is an uncertainty in the Schottky barrier height, which makes it difficult to use Mott's – Schottky rule to experimentally determine the electronic affinity of Si@O@Al.

2.2. Structural model of SSLIB Si@O@Al—LiPON—LiCoO$_2$

Experimental Nyquist diagrams of Ti(200 nm)Si@O@Al(0.3 μm)—LiPON(1 μm)—LiCoO$_2$(1 μm) —Ti(10 μm), where Ti(10 μm) — substrate, are shown in Fig. 4. The general pattern of curve change with increasing temperature is a decrease in the real and imaginary parts of the impedance while maintaining the general appearance of the curves. In the area of low temperatures (from −20 to −10°C), no significant difference is observed between the diagrams in the charged and discharged states. In the area of positive temperatures in the charged state, three arcs are clearly distinguishable in the diagram (one arc in the high-frequency area is not visible in Fig. 4), whereas only two arcs are present in the discharged state. The following structural model has been proposed to describe the frequency dependence of the impedance of the functional layers and interfaces.

The structure of SSLIB is formed by three functional layers — negative electrode (NE), electrolyte (Elt) and positive electrode (PE) and two electrode−electrolyte interfaces (Elt−Eld). Therefore, a sequence of R_n−CPE$_n$ chains is considered below as a structural model of SSLIB (Fig. 5), where R_n — the active resistance of the element, CPE$_n$ — a constant phase element whose impedance is of the form $Z_n = \mathrm{A}_n(j\omega)^{-\alpha}$. The parameter A may have different physical meaning depending on the non-ideality factor $\alpha \in [-1, 1]$. In Fig. 5 in the structural model of each layer and interface, there is an active resistance R_n, which limits the area of variation α to the segment [0.5,1]. In this range, CPE describes the resistance to diffusive

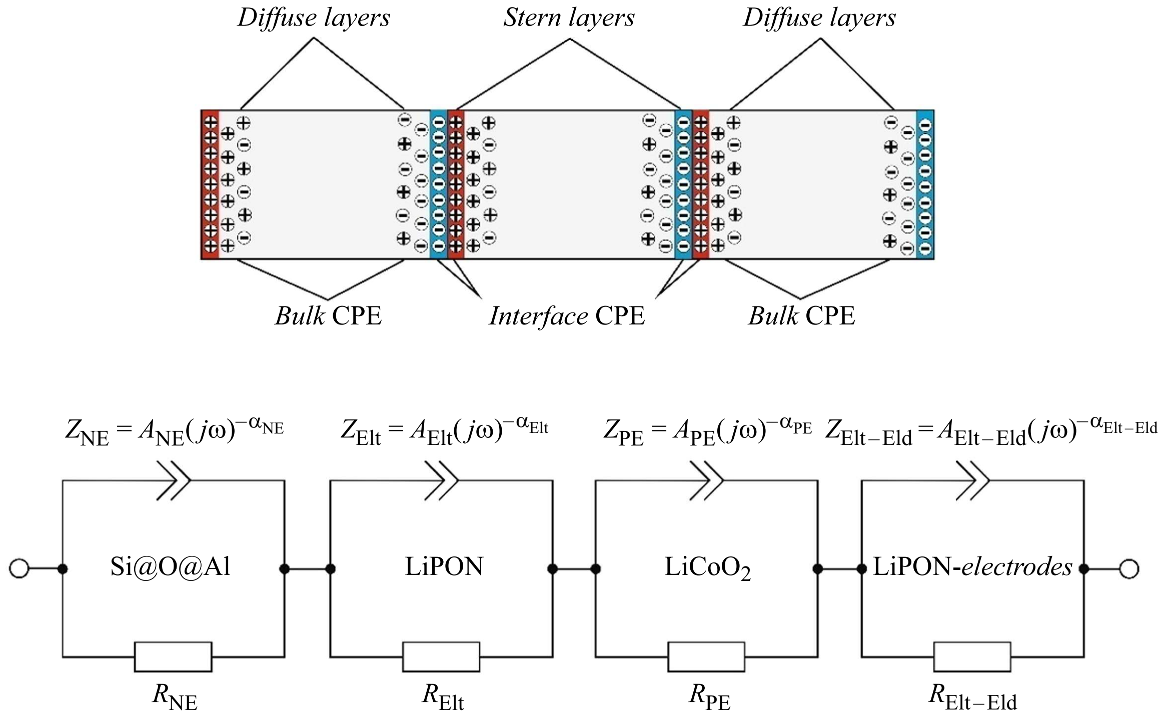

Figure 5. SSLIB structural model

charge transfer and sorption current (displacement current). Therefore, the term diffusion-sorption conductivity is used hereafter. Here, the constant phase elements are used solely for the convenience of comparing the structural model in Fig. 5 with the structural models of other information sources, which consist mainly of constant phase elements.

It is further assumed that the $CPE_{Elt-Eld}$ can be considered as a capacitor formed by a dense part of an electrical double layer or Stern layer, with diffusion leakage. The active resistance of the $R_{Elt-Eld}$ models the drift transfer of lithium across the interface. The remaining $R-$ CPE chains in fig. 5 model the impedance of the LiPON and electrodes. In the LiPON chain, the R_{Elt} element describes the resistance to drift transport of lithium ions, and CPE_{Elt} — diffusive transport of Li in the electrolyte layer and the displacement current through the capacity formed by the diffuse areas of the electric double layer. In [19], a detailed LiPON model was considered, which is here replaced by a more formal model for ease of comparison with the results of other works. In Si@O@Al and $LiCoO_2$ chains, the resistances R_{NE} and R_{PE} are responsible for both ionic and hole drift conductivity, while CPE_{NE} and CPE_{PE} — for diffusion-sorption conductivity.

Similar circuits were used to simulate the impedance of an SSTFLIB of the Li–LiPON–$LiCoO_2$ electrochemical system [22–24] and lithium cobaltite [25]. However, they differ in certain respects. For example, in paper [21], there are no structural elements modeling the impedance of the electrodes. In this case of [21], a generalized Warburg element is introduced into the LiPON—$LiCoO_2$ interface circuit in series with the active resistance. This means that drift and diffusive charge transfer occur sequentially, which is not clear in the case of the interface. The impedance of interfaces of a solid electrolyte and electrodes is taken into account in the structural model in [22]. Notably, the diffusion properties of an electrolyte are modeled by a separate Warburg element, which is connected in series with structural elements of all functional layers. A capacitor, which accounts for the current in a battery at constant voltage, is introduced into the structural model to simulate the so-called electrochemical capacity. This capacity is neglected in the model in Fig. 5 due to the boundedness of limited frequency range.

The real and imaginary parts of impedance of the structural model in Fig. 5 take the form

$$\mathrm{Re}(\hat{Z}) = \sum_{n=1}^{4} R_n \frac{R_n A_n \omega^{\alpha_n} \cos\left(\alpha_n \frac{\pi}{2}\right) + A_n^2}{R_n^2 \omega^{2\alpha_n} + 2R_n A_n \cos\left(\alpha_n \frac{\pi}{2}\right)\omega^{\alpha_n} + A_n^2}, \quad (1)$$

$$\mathrm{Im}(\hat{Z}) = -j \sum_{n=1}^{4} \frac{R_n^2 A_n \omega^{-\alpha_n} \sin\left(\alpha_n \frac{\pi}{2}\right)}{R_n^2 + 2R_n A_n \omega^{-\alpha_n} \cos\left(\alpha_n \frac{\pi}{2}\right) + A_n^2 \omega^{-2\alpha_n}}, \quad (2)$$

where $R_1 = R_{NE}$, $A_1 = A_{NE}$, $\alpha_1 = \alpha_{NE}$, $R_2 = R_{Elt}$, $A_2 = A_{Elt}$, $\alpha_2 = \alpha_{Elt}$, $R_3 = R_{PE}$, $A_3 = A_{PE}$, $\alpha_3 = \alpha_{PE}$, $R_4 = R_{Elt-Eld}$, $A_4 = A_{Elt-Eld}$, $\alpha_4 = \alpha_{Elt-Eld}$. The values of the listed parameters, at which the best agreement with the experimental data is achieved, are given in Table 2. The accuracy of the approximation of the experimental Nyquist diagrams in the

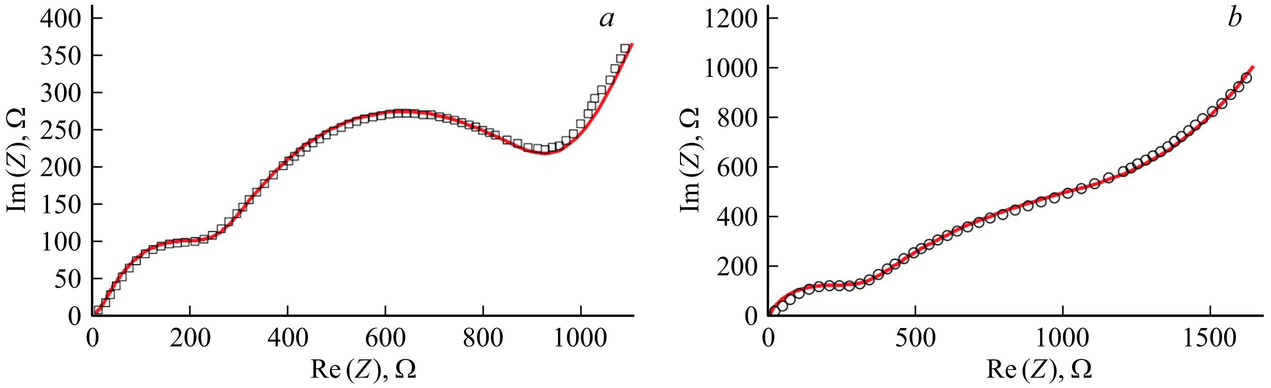

Figure 6. Results of fitting the impedance parameters of the SSLIB: *a* — for a charged battery, *b* — for a discharged battery

Table 2. Parameters of approximating dependences (1) and (2) at 20°C

Parameter	Charged	Discharged
R_{Elt}, Ω	15	20
A_{Elt}, $\Omega/\mathrm{s}^{1/2}$	$2.2 \cdot 10^4$	$2.2 \cdot 10^4$
α_{Elt}	0.5	0.5
R_{NE}, Ω	670	1170
A_{NE}, $\Omega/\mathrm{s}^{\alpha_{\mathrm{NE}}}$	$2 \cdot 10^4$	$2.2 \cdot 10^4$
α_{NE}	0.79	0.66
R_{PE}, Ω	230	270
A_{PE}, $\Omega/\mathrm{s}^{\alpha_{\mathrm{PE}}}$	$2.2 \cdot 10^5$	$2.2 \cdot 10^4$
α_{PE}	0.77	0.78
$R_{\mathrm{Elt-Eld}}$, Ω	10^5	10^5
$A_{\mathrm{Elt-Eld}}$, $\Omega/\mathrm{s}^{\alpha_{\mathrm{Elt-Eld}}}$	570	4500
$\alpha_{\mathrm{Elt-Eld}}$	0.67	0.77

charged and discharged states at temperature 20°C (Fig. 6) is illustrated by plots of dependencies (1) and (2).

The values of fitting parameters provide data on changes in functional SSLIB layers induced by their lithiation or delithiation. In particular, the active resistance of lithiated Si@O@Al is almost two fold lower than that of unlithiated Si@O@Al (Table 2). Both active resistance values are three orders of magnitude higher than the true Si@O@Al resistance value of $\sim 1\,\Omega$ for this structure. An explanation of this artefact will be given below. The ionic conductivity of Si@O@Al is of diffusion-capacitive nature as indicated by the non-ideality factor 0.79–0.66. Moreover, sorption current dominates in the lithiated state, and in delithiated — diffusive transfer of lithium, which may indicate an increase in the capacitance of the diffusive part of the EDL in the lithiated state. The parameter A_{NE} is essentially unchanged when the lithium concentration is changed. Note that in the Cole and Cole [26] model, the parameter *A* is expressed through such system parameters as ε — the dielectric constant of the medium, τ — the relaxation time of polar molecules, and C_0 — the capacitance of the air capacitor $A = \tau^{1-\alpha}/[\varepsilon(0)-\varepsilon_\infty]C_0$. When CPE is extended to electrochemical systems, this relationship becomes useless in interpreting the parameter *A*. In this case, a detailed structural model is needed, not a universal one, which is the constant phase element.

In [27], it is shown that the resistance of $\mathrm{Li}_{1-x}\mathrm{CoO}_2$ is strongly dependent on lithium deficiency „*x*“. The conductivity increase was attributed in [28,29] to the formation of holes in the 3*d* band. Despite this property of lithium cobaltite, the active resistance in the charged and discharged states is almost the same. Moreover, the resistivity of $\mathrm{Li}_{1-x}\mathrm{CoO}_2$ significantly exceeds the work [27] data. The ionic conductivity of lithium cobaltite has a diffusion-sorption nature, which is characterized by the non-ideality factor 0.77–0.78 (Table 1). Since the non-ideality factor is independent of lithium deficiency, we can say that the ratio between displacement current and diffusion current is independent of lithium deficiency. However, the A_{PE} — amplitude of diffusion-sorption resistance in the lithiated state ($x = 0$) isan magnitude of order higher than in the delithiated state. Finally, the resistance of $R_{\mathrm{Elt-Eld}}$ is found to be high enough $\sim 10^5\,\Omega$, which allows us to attribute this resistance to the electrode-electrolyte junction. It is noteworthy that the diffusion-sorption resistance of the transition in the discharged state is an order of magnitude higher than in the charged state.

Thus, by measuring the impedance of the multilayer Ti—LiCoO_2—LiPON—Si@O@Al—Ti battery structure and modeling it, the resistances of the functional layers and charge transfer mechanisms have been determined. The resistances of the positive and negative electrodes were found to be much higher than those reported in the literature. The following is a description of experiments to measure the resistance of electrode materials and to find out the causes of impedance spectroscopy artefacts.

2.3. Influence of varistor effect and nonohmicity of contacts on the results of impedance spectroscopy of SSLIB

The most important characteristic of a SSLIB is the resistance of the functional layers and interfaces. Both this and the other, as shown above, depend on the degree of lithiation and the potential on the battery. The results of conductivity measurements *in situ* performed by electrochemical impedance spectroscopy (EIS) can be strikingly different from those of the layers within the structures. For this reason, interpretation of SSLIB impedance spectra can lead to artefacts. For example, in Section. 2, a structural model of SSLIB Ti—$LiCoO_2$—LiPON—Si@O@Al—Ti was proposed (Fig. 5), which describes the EIS results well. At the same time, the resistances of electrodes obtained by fitting were much higher than the ones determined using cyclic voltammetry (CV) for the Ti—Si@O@Al—Ti structure [12] and the EIS resistances for bulk $LiCoO_2$ [27]. The overestimation of resistance may be due to the junction metal – semiconductor, which in the framework of the structural model (Fig. 5) was not allocated in a separate structural element, as, however, and in similar studies of other authors [20–23]. In order to verify this assumption, we measured the impedance and CVCs of test Ti—Si@O@Al—Ti and Ti—$LiCoO_2$—Ti structures.

The resistance of the Ti—Si@O@Al—Ti structure under zero bias is $R = \max\mathrm{Re}(Z) = 7.52\,\mathrm{k\Omega}$, whereas the resistance of the same structure under a bias of 1 V reported in [12] was just $6.26\,\Omega$. The indicated discrepancy is attributable to the varistor effect and the resistance of a metal – semiconductor contact. In [12] it was shown that the CVC of the Ti–Si@O@Al junction at reverse bias (plus on the metal) has an exponential character. As a result, at zero bias, the amplitude of current oscillations has a magnitude of the order of the saturation current and accordingly the real part of the impedance has a maximum value. As the bias increases, the amplitude of the current oscillation increases and the resistance of the test structure decreases accordingly.

Based on the above, as the bias voltage increases, the values should decrease due to decreasing contact resistance and varistor effect. The sign of this bias voltage is insignificant, since one junction will be biased in the forward direction and its characteristic will remain linear. The second junction will be biased in the backward direction, i.e., into the area with a steeper CVC slope. The differential contact resistance will decrease as a result, and the circle in a Nyquist plot will contract. The fairness of the above is illustrated by the plot of the dependence of the active resistance $\max\mathrm{Re}(Z)$ on the bias voltage U_b, shown in Fig. 7.

The analytical expression for the experimental dependence of $\max\mathrm{Re}[Z(U_b)]$ can be found using the relation

$$I = I_s\left\{\exp\left[(U_b - U_V)/\phi\right] - 1\right\}, \tag{3}$$

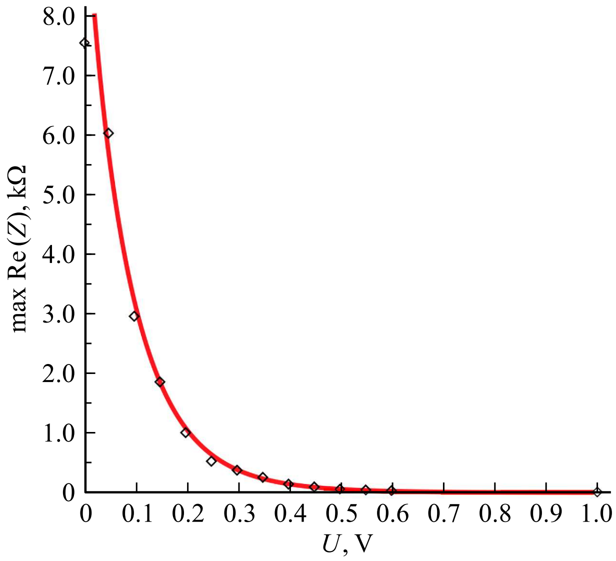

Figure 7. Experimental dependence $\max\mathrm{Re}\,Z(U_b)$ (rhombuses) and approximating dependence (solid curve) at parameters $I_S = 2.75\cdot 10^{-5}\,\mathrm{A}$, $b = 0.68$, and $R_0 = 3.0\,\Omega$. Parameters $R^* = 1.56\,\Omega\cdot\mathrm{A}^{1-\alpha}$ and $\alpha = 0.45$ were taken from [4].

which is more conveniently represented as

$$U_b - U_V = \phi\ln(1 + I/I_S), \tag{4}$$

where $\phi = k_{\mathrm{B}}T/q$, I_S — saturation current, U_b — displacement voltage, U_V — voltage drop across the volume. Taking the Si@O@Al varistor effect into account, one may write $U_V = R^*I^\alpha + R_0I$, where R^* is a coefficient with a dimension of $\Omega\cdot\mathrm{A}^{1-\alpha}$. The current dependence of the bias then takes the form

$$U_b = \phi\ln(1 + I/I_s) + R^*I^\alpha + R_0I. \tag{5}$$

Since the experimental value of $\max\mathrm{Re}[Z(U_b)]$ — is the differential resistance of the entire test structure, it corresponds to the derivative of U_b by the current of

$$R(U_b) = \frac{dU_b}{dI} = \frac{\phi}{I_s + I} + \frac{\alpha R^*}{I^{1-\alpha}} + R_0. \tag{6}$$

In expression (6), the current I should be replaced by expression (3), in which the unknown function $U_V(U_b)$ can be decomposed into a power series $U_V(U_b) = \alpha U_b + \beta U_b^2 + \ldots$. In this case, as will be shown below, the linear term $U(U_b) \approx \alpha U_b$ is sufficient:

$$R(U_b) = \frac{\phi}{I_S}\exp\left[\frac{(b-1)U_b}{\phi}\right] + \frac{\alpha R^*}{I_S}\left\{\exp\left[\frac{(1-b)U_b}{\phi}\right]\right\}^{\alpha-1} + R_0. \tag{7}$$

In Fig. 7, which shows the graph of the function $\max\mathrm{Re}[Z(U_b)]$, it can be seen that the experimental points of $\max\mathrm{Re}(Z)$ lie fairly well on the curve (7). The

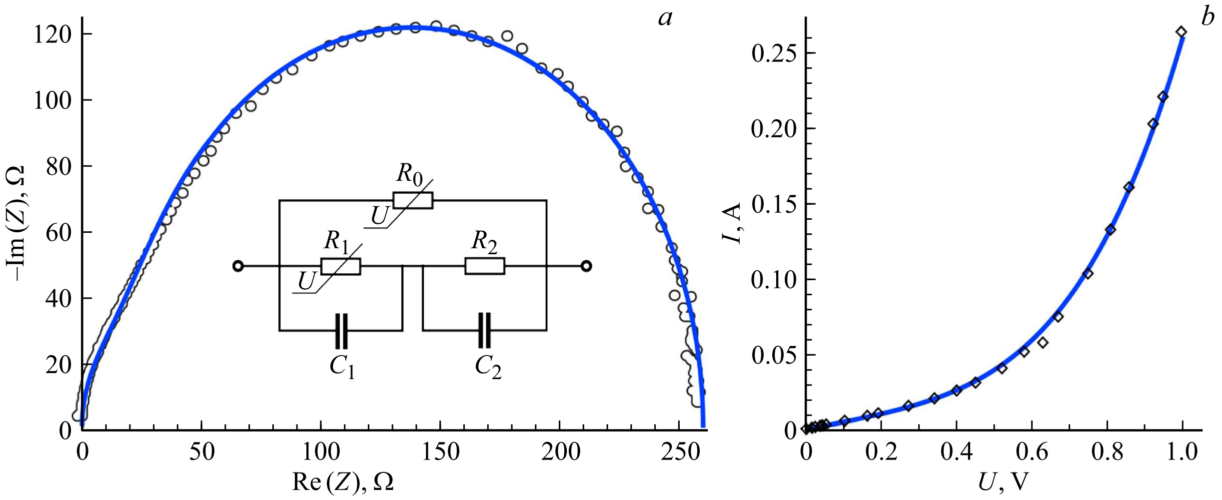

Figure 8. *a* — Nyquist plot for the Ti—LiCoO$_2$—Ti test structure and its structural model. Frequency band 0.5 Hz−500 kHz. Circles — experimental points, solid line — approximating curve. The Nyquist diagram is generated with the structural model parameters $R_0 = 17.2\,\text{M}\Omega$, $R_1 = 240\,\Omega$, $R_2 = 20\,\Omega$, $C_1 = 2.0 \cdot 10^{-6}$ F, $C_2 = 2.0 \cdot 10^{-6}$ F. The resistances of the R_1, R_2 varistors are given for bias voltage 5 mV. *b* — CVC of the Ti—LiCoO$_2$—Ti test structure: rhombuses — experimental points; solid line — approximating relationship (10).

parameters of the approximating dependence are given in the caption to Fig. 7. The residual resistance $R_0 = 3\,\Omega$ corresponds to the minimum experimental resistance value $\max \text{Re}[Z(U_b)]$. From the above, it follows that when U_b increases, the value of $\max \text{Re}(Z)$ actually decreases due to the reduction of the Schottky barrier on the Si@O@Al side and the varistor effect Si@O@Al.

Fig. 8, *a* shows the Nyquist diagram constructed from measurements of the Ti—LiCoO$_2$—Ti test structure. The diagram consists of two reasonably well-defined half-circles that can be generated using two contours R_1C_1 and R_2C_2 (insert in draw 8, *a*). The resistor R_0 models the percolation skeleton of nanocrystalline lithium cobaltite, and at a probe voltage amplitude of 5 mV can be assumed to be infinity. This resistor is introduced into the structural model to reconcile the impedance spectroscopy results with the cyclic voltammetry data. The Nyquist diagram corresponding to the structural model in the inset of Fig. 8, *a* is shown as a solid line. The best-fit parameters of the model are $R_0 = 17.2\,\text{M}\Omega$, $R_1 = 240\,\Omega$, $R_2 = 20\,\Omega$, $C_1 = C_2 = 2 \cdot 10^{-6}$ F. Note that the resistor $R_1 = 240\,\Omega$ corresponds with good accuracy to the resistance of the positive electrode of the SSLIB in Table 1.

To confidently interpret the impedance spectroscopy results, the CVCs of the Ti—LiCoO$_2$—Ti test structure were investigated. CVC were recorded in the range from −1 to +1 V at two sweep rates 5 and 10 mV/s. As shown by the CVC analysis, the dependence of $I(U)$ is nonlinear, but not exponential. This means that the Ti–LiCoO$_2$ is ohmic contact and the lithium cobaltite film is a varistor. Ohmic contact is possible because the Fermi level of LiCoO$_2$ lies 1 eV below the Fermi level of titanium [30]. In this case, the semiconductor zones are bent upwards, and an enriched electron layer and a depleted hole layer are formed in the contact area. The varistor R_0 in Fig. 8, *a* models the electronic conductivity of lithium cobaltite, and the varistor R_1 and resistor R_2 model hole volumetric and depletion layer conductivity, respectively. The varistor effect of lithium cobaltite volume is accounted for using the following ratios:

$$U_b = U_V = R_0^* I_1^\alpha \tag{8}$$

for electronic conduction and

$$U_b = U_V + R_2 I_2 = R_2^* I_2^\alpha + R_2 I_2 \tag{9}$$

for hole conduction, where U_b is bias voltage. From relations (8), (9) follows expressions for the total current

$$I = I_1 + I_2 = \left(\frac{U_b}{R_0^*}\right)^{1/\alpha} + \frac{U_b}{R_1^* I^{\alpha-1} + R_2}. \tag{10}$$

Fig. 8, *b* shows the plot of the implicit function (10) (solid line) and the experimental CVC (dots). The best approximation of the dependence (10) is given at $R_0^* = 1.5\,\Omega \cdot \text{A}^{1-\alpha}$, $R_1^* = 0.034\,\Omega \cdot \text{A}^{1-\alpha}$, $R_2 = 20\,\Omega$ and $\alpha = 0.26$. The resistances of $R_0(U_b)$ and $R_1(U_b)$ in Fig. 8, *a* at $U_b = 5$ mV are 17.2 MΩ and 240 Ω, respectively.

The concept of resistivity may be used to characterize the resistance of materials with a varistor effect. By definition, the expression for resistivity in this case is $\rho = (R^* S^\alpha / h) j^{\alpha-1} + R_0 S/h$ (or, in a more compact form, $\rho = \beta j^{\alpha-1} + \rho_0$), where j is the current density and S and h are the film area and thickness. Measurements of resistivity then boil down to determining the values of parameters β, ρ_0 and α. For Si@O@Al, $R^* = 1.56\,\Omega \cdot \text{A}^{1-\alpha}$, $\beta = 8.67 \cdot 10^4\,\Omega \cdot \text{A}^{1-\alpha} \cdot \text{cm}^{2\alpha-1}$, $\alpha = 0.45$. For LiCoO$_2$, $R_1^* = 0.082\,\Omega \cdot \text{A}^{1-\alpha}$, $\beta = 1.640 \cdot 10^3\,\Omega \cdot \text{A}^{1-\alpha} \cdot \text{cm}^{2\alpha-1}$, $\alpha = 0.26$.

Conclusion

Our findings suggest the following conclusions. The use of semiconductor materials such as silicon nanocomposite, vanadium pentoxide and lithium cobaltite can increase the specific capacitance and stability of SSLIB. But there are a number of problems associated with the nonohmicity of metal – semiconductor contacts and the varistor effect in the electrode materials. This is first of all true for silicon, since the M—$LiCoO_2$ contacts are ohmic (there are no reliable data regarding M—$Li_xV_2O_5$). In the contact area of M—a-Si(Al), a Schottky barrier is formed, which creates an additional voltage drop on the battery structure of 1.5 V when the conduction type changes from hole to electronic. This results in an additional internal resistance, which at a charge current of 0.1 mA for a battery with cathode $Li_xV_2O_5$ is $\sim 15\,k\Omega$. Another reason for the increase in internal resistance upon charging may be the compensation of the acceptor impurity Al by the donor impurity Li. At determined charge stage, the a-Si(Al,Li) solid solution becomes a compensated semiconductor with high resistivity.

In addition to the contact phenomena listed above, varistor effects make a hard-to-measure contribution to resistance. So far, this effect has been found in Si@O@Al and $LiCoO_2$, but it is likely a general property of semiconductor electrodes having nanocrystalline structure. At low current, the resistance of a film of electrode material with an area of 1 cm^2 and a thickness of $0.5\,\mu m$ reaches tens MΩ. When measuring the impedance of SSLIB and functional layers *in situ*, the nonohmicity of the metal–electrode contact and the varistor effect can lead to significant measurement error, and the active resistance values can be overestimated by two–three orders of magnitude.

Thus, SSLIBs based on semiconductor materials have different contact resistances of the down conductor – electrode at different stages of charge. Under different charge modes, the internal resistance of the SSLIB will also vary due to the varistor effect. All of the above effects introduce uncertainty in determining the state of charge (SoC) of the battery and must be taken into account when developing models SSLIB.

Funding

The work was carried out within the framework of the State assignment of the Yaroslavl branch of the K. A.Valiev Institute of Physics and Technology of the Russian Academy of Sciences of the Ministry of Education and Science of the Russian Federation on the topic №FFNN-2022-0017 on the equipment of the Center Facilities Sharing „Diagnostics of micro- and nanostructures“.

Conflict of interest

The authors declare that they have no conflict of interest.

References

[1] N.F. Mendoza. *Flexible Battery Market to hit 500 Million in 2030* [Electronic source] Available at: https://www.techrepublic.com/article/flexible-battery-market-to-hit-500-million-in-2030 (date of access: 12.10.2020)

[2] J.B. Bates, N.J. Dudney, B.J. Neudecker, F.X. Hart, H.P. Jun, S.A. Hackney. J. Electrochem. Soc., **147**, 59 (2000). DOI: 10.1149/1.1393157

[3] Y.N. Zhou, M.Z. Xue, Z.-W. Fu. J. Power Sources, **234**, 310 (2013). DOI: 10.1016/j.jpowsour.2013.01.183

[4] X. Zuo, J. Zhu, P. Müller-Buschbaum, Y.-J. Cheng. Nano Energy, **31**, 113 (2017). DOI: 10.1016/j.nanoen.2016.11.013

[5] K. Feng, M. Li, W. Liu, A.G. Kashkooli, X. Xiao, M. Cai, Z. Chen. Small, **14**, 1702737 (2018). DOI: 10.1002/smll.201702737

[6] W.-J. Zhang. J. Power Sources, **196**, 13 (2011). DOI: 10.1016/j.jpowsour.2010.07.020

[7] J.R. Szczech, S. Jin. Energy Environ. Sci., **4**, 56 (2011). DOI: 10.1039/C0EE00281J

[8] B. Liang, Y. Liu, Y. Xu. J. Power Sourc., **267**, 469 (2014). DOI: 10.1016/j.jpowsour.2014.05.096

[9] A.V. Metlitskaya, A.A. Mironenko, N.F. Nikol'skaya, V.V. Odinokov, G.Ya. Pavlov, D.E. Pukhov, A.S. Rudyi, A.M. Skundin, V.A. Sologub, I.S. Fedorov, A.B. Churilov. Russ. Microelectron., **45** (4), 285 (2016). DOI: 10.1134/S1063739716030021

[10] A.A. Mironenko, I.S. Fedorov, A.S. Rudy, V.N. Andreev, D.Yu. Gryzlov, T.L. Kulova, A.M. Skundin. Monatshefte fur Chemie-Chemical Monthly, **150** (10), 1753 (2019). DOI: 10.1007/s00706-019-02497-1

[11] A.S. Rudy, A.A. Mironrenko, V.V. Naumov, A.B. Churilov. Tech. Phys. Lett., **48** (6), 63 (2022). DOI: 10.21883/TPL.2022.06.53794.19188

[12] A.S. Rudy, A.B. Churilov, A.A. Mironrenko, V.V. Naumov, S.V. Kurbatov, E.A. Kozlov. Tech. Phys. Lett., **48** (9), 7 (2022). DOI: 10.21883/TPL.2022.09.55072.19276

[13] T.L. Kulova, A.A. Mironenko, A.S. Rudy, A.M. Skundin, *All Solid State Thin-Film Lithium-Ion Batteries. Materials, Technology, and Diagnostics* (CRC Press. Taylor & Francis Group, LLC, London, NY., 2021), DOI: 10.1201/9780429023736

[14] L.A. Mazaletsky *Issledovaniye vliyaniya struktury i fazovogo sostava nanokompozitov na osnove kremniya na protsessy vnedreniya i ekstraktsii litiya. Kand. diss.* (MIFI, M., 2022), 134 p.

[15] M. Grundmann *The Physics of Semiconductors. An Introduction Including Nanophysics and Applications, Graduate Texts in Physics* (Springer Nature Switzerland AG 2021), DOI: 10.1007/978-3-030-51569-0

[16] D.A. Drabold, U. Stephan, J. Dong, S.M. Nakhmanson. J. Mol. Graphics Mod., **17** (5–6), 285 (1999). DOI: 10.1016/S1093-3263(99)00036-4

[17] B.A. Golodenko, A.B. Golodenko. Vestnik VGUIT **2**, 65 (2014). https://cyberleninka.ru/article/n/modelirovanie-elektronnoy-struktury-i-raschyot-osnovnyh-elektro-fizicheskih-parametrov-amorfnogo-kremniya

[18] B.A. Golodenko, A.B. Golodenko. Nano- i mikrosistemnaya tekhnika, **11**, 148 (23) (2012) (in Russian). http://www.micro-systems.ru/files/publ/article201211p23-27.pdf

[19] A. Rudy, A. Mironenko, V. Naumov, A. Novozhilova, A. Skundin, I. Fedorov. Batteries, **7** (2), 21 (2021). DOI: 10.3390/batteries7020021

[20] Y. Iriyama, T. Kako, C. Yada, T. Abe, Z. Ogumi. J. Power Sourc., **146** (1–2), 745 (2005). DOI: 10.1016/j.jpowsour.2005.03.073

[21] Y. Iriyama, T. Kako, C. Yada, T. Abe, Z. Ogumi. Solid State Ionics, **176** (31–34), 2371 (2005). DOI: 10.1016/j.ssi.2005.02.025

[22] S.D. Fabre, D. Guy-Bouyssou, P. Bouillon, F.Le Cras, C. Delacourta. J. Electrochem. Soc., **159** (2) A104 (2012). DOI: 10.1149/2.041202jes

[23] S. Larfaillou, D. Guy-Bouyssou, F. Le Cras, S. Franger. ECS Transactions, **61** (27), 165 (2014). DOI: 10.1149/06127.0165ecst

[24] D. Aurbach, M.D. Levi, E. Levi, H. Teller, B. Markovsky, G. Salitra, U. Heider, L. Heider. J. Electrochem. Soc., **145** (9), 3024 (1998). DOI: 10.1149/1.1838758

[25] R.I. Korneikov, V.V. Efremov, V.I. Ivanenko, K.A. Kesarev. Russ. J. Electrochem. **57** (5), 499 (2021). DOI: 10.1134/S1023193521050074

[26] K.S. Cole, R.H. Cole. J. Chem. Phys., **9** (4) 341 (1941). DOI: 10.1063/1.1750906

[27] D.G. Kellerman, V.R. Galakhov, A.S. Semenova, Ya.N. Blinovskov, O.N. Leonidova. Phys. Solid State, **48** (3), 548 (2006). DOI: 10.1134/S106378340603022X

[28] E. Plichta, M. Solomon, S. Slane, M. Uchiyama, D. Chua, W.B. Ebner, H.W. Lin. J. Power Souces, **21** (1), 25 (1987). DOI: 10.1016/0378-7753(87)80074-5

[29] K. Wang, J. Wan, Y. Xiang, J. Zhu, Q. Leng, M. Wang, L. Xu, Y. Yang. J. Power Souc., **460**, 228062 (2006). DOI: 10.1016/j.jpowsour.2020.228062

[30] M.W. Swift, Y. Qi. Phys. Rev. Lett., **122**, 167701 (2019). DOI: 10.1103/PhysRevLett.122.167701

Translated by Y.Deineka